ORIGINAL PAPER

Improved electrochemical properties of Sn-doped TiO_2 nanotube as an anode material for lithium ion battery

Caiyan Yu · Ying Bai · Dong Yan · Xiaoge Li · Weifeng Zhang

Abstract Anatase TiO_2 nanotube was doped with different contents of Sn (3, 5, and 7 at.%) through sol-gel method and subsequent hydrothermal process. X-ray diffraction (XRD), Raman spectroscopy, X-ray photoelectron spectroscopy (XPS), field emission scanning electron microscopy (FESEM), high-resolution transmission electron microscopy (HRTEM), Brunauer-Emmett-Teller (BET), and Hall effect measurement are utilized to characterize the structures, components, chemical environments, morphologies, specific areas, and electronic conductivities of the samples. The investigation in cycling performances demonstrates that 5 at.% Sn-doped TiO_2 nanotube exhibits the best cycling stability, with specific capacity of 386 mAh g^{-1} and coulombic efficiency of 99.2 % after 50 cycles at 0.1 C, much higher than those of the other Sn-doped samples and pristine TiO_2 nanotube. The improved electrochemical performances of Sn-doped TiO_2 nanotube are attributed to the increase of electronic conductivity and therefore enhance the reversible capacity of the material.

C. Yu · Y. Bai · D. Yan · X. Li · W. Zhang (✉)
Key Laboratory of Photovoltaic Materials of Henan Province and School of Physics and Electronics, Henan University, 475004 Kaifeng, People's Republic of China
e-mail: wfzhang@henu.edu.cn

W. Zhang
e-mail: wfzhang6@163.com

Introduction

Lithium ion battery (LIB) is a prevailing portable power source due to its higher volumetric and gravimetric energy densities compared with those of other rechargeable battery systems, which has been widely used in various portable electronic devices including cellular phones, laptop computers, and camcorders. Notwithstanding, safety problem and power density of LIB have not yet reached the requirements of high-powered devices, especially for electric vehicles (EV) and plug-in hybrid electric vehicles (PHEV) [1–3]. Among the potential anode substitutes, TiO_2 has been widely investigated as a candidate with high-rate performance, stable capacity retention, and safe operation during charge/discharge process. And, as a multifunctional material, it has also been widely studied and used in various fields, such as photocatalysts, dye-sensitized solar cell, and semiconductors [4, 5].

Apart from these advantages, anatase TiO_2 exhibits a flat plateau and high lithium insertion potential at approximately 1.7 V, which avoids the formation of surface electrolyte interface (SEI) layer [6, 7]. It is well known that the electrochemical performances of anode materials are highly dependent on their morphologies, surface characteristics, and particle sizes. Recently, nanosized TiO_2 with special morphologies, such as mesoporous microsphere [8], nanofibers [9], and nanoflower [10], has shown improved capacities and cycle lives due to shortened diffusion distance of lithium ion and increased specific area [8–15]. Among these nanostructured materials, TiO_2 nanotube with larger specific area, leading to contact with the electrolyte adequately, is beneficial to improve the electrochemical properties. In addition, the spaces inside the TiO_2 nanotube also eliminate the stress of volume change effectively during repeated alloying and dealloying, hence contributing to excellent electrochemical performances.

However, TiO_2 anode has intrinsically low electronic conductivity, which limits its application for high power output. Doping represents an important technique to effectively modify the mechanical, optical, and electronic properties of TiO_2 bulk materials. The other prominent advantage of doping is that the crystal structure of host material can be modified by controlling the dopant concentration [16, 17]. Introducing an ion with the same valence state with Ti^{4+} may lead to the modification of the particle size by a nucleation effect [18], which means that the anatase phase can be formed more rapidly. On the other hand, the ionic radius of Sn^{4+} (0.069 nm) is quite close to that of Ti^{4+} (0.0606 nm) [19], which will decrease the lattice mismatch in the most extent after the same valence state Sn^{4+} doping and will remain the original anatase structure of TiO_2.

In fact, it has been reported that tin-doped samples of $Ti_{0.95}Sn_{0.05}O_2$ nanoparticles [16] and $Ti_{2/3}Sn_{1/3}O_2$ nanocrystals [17] exhibit improved electronic conductivity, indicating the influence of partial substitution of titanium by tin in the anatase framework. Meanwhile, Sn-doped TiO_2 nanotube fabricated by anodization of cosputtered Ti-Sn thin film [20] has been reported. However, it is difficult to realize industrialization due to the complexity of the process and thus the high cost of as-prepared material.

In our study, power samples of TiO_2 nanotube doped with Sn (3, 5, and 7 at.%) were prepared and studied for the first time. In the preparation process, the facile sol-gel method and subsequent hydrothermal process are applied, which are easy to be conducted. In this work, the electrochemical performances after Sn doping are superior to previous reports focusing on Sn-doped anatase TiO_2. Further, the impact of microstructures on electrochemical properties is investigated and compared. As a result, Sn-doped TiO_2 nanotube demonstrates much improved electrochemical reversibility, which is attributed to the increase of electronic conductivity.

Experimental

Sn-doped anatase TiO_2 nanotube was synthesized through sol-gel method and subsequent hydrothermal process. First, 5 at.% Sn-doped TiO_2 nanoparticles were synthesized using sol-gel method as described in the following: 5 ml of $Ti(OC_4H_9)_4$ was dissolved in 30 ml of ethanol to get solution (I). Meanwhile, 0.25 g of $SnCl_4 \cdot 5H_2O$ was added to 10 ml of ethanol and dispersed by an ultrasonicator for 10 min. Afterward, 2 ml of acetylacetone and 10 ml of ethanol were added in under magnetic stirring. The obtained solution was signed as solution (II). Then, the solution (I) was slowly dropped into the solution (II) under constant stirring to get the solution. After aged for 48 h, the gel was dried at 70 °C for 36 h and then calcined at 400 °C for 2 h in air. Second, the nanoparticles were mixed with 10 mol L^{-1} NaOH aqueous solution. The suspension was then converted to a Teflon autoclave and experienced a subsequent hydrothermal reaction at 120 °C for 24 h. After cooling to room temperature, the product was harvested by centrifugation and rinsed for several times and then dried at 70 °C under vacuum overnight. The powder was finally annealed at 400 °C for 2 h under flowing argon to obtain Sn-doped TiO_2 nanotube. To be strict, the preparation processes of pristine TiO_2 nanotube and Sn-doped TiO_2 nanotubes were the same as described above except different contents of $SnCl_4 \cdot 5H_2O$.

Surface morphology and microstructure of samples were characterized by field emission scanning electron microscopy (FESEM, JSM-7001 F, JEOL) and high-resolution transmission electron microscopy (HRTEM, JEM-2010, JEOL). The specific surface areas were evaluated with a BELSORP-mini surface analyzer (V-Sorb 2800, Beijing, Gold App) based on the Brunauer-Emmett-Teller (BET) multipoint method and N_2 physisorption at room temperature. Adsorption-desorption isotherm measurements were used to determine the porosity and pore size distribution using the Barrett-Joyner-Halenda (BJH) method. X-ray diffraction (XRD) measurements were performed on a diffractometer (DX-2700, Fangyuan) with Cu Kα radiation with λ=1.54145 Å. Raman spectra were recorded on a Raman spectrometer (RM-1000, Renishaw) with 632.8 nm He-Ne laser as irradiation source. The X-ray photoelectron spectroscopy (XPS) analysis was carried out on Kratos Axis Ultra using a monochromatic Al Kα radiation, and the binding energies (BEs) were calibrated with those of C1s at 284.8 eV as the reference. Electronic conductivity of the samples was performed with Hall effect measurement system (HMS-3000, Ecopia).

The electrochemical measurements were carried out using two-electrode button-type cells with pure lithium metal as both the reference electrode and the counter electrode at room temperature. The working electrode consisted of active material, carbon black, and binder (PVDF) in a weight ratio of 70:15:15. The slurry was coated on copper foil current collector and then dried in a vacuum oven at 120 °C overnight, finally cut into square electrode sheets (8×8 mm^2). Celgard 2400 was used as the separator membrane, and the electrolyte used was 1 M $LiPF_6$ dissolved in a mixture of diethyl carbonate (DEC) and ethylene carbonate (EC) with 1:1 volume ratio. The test cells were assembled in purified Ar-filled glove box (Super1220/750, Mikrouna) with concentrations of oxygen and moisture below 1.0 ppm. Cyclic voltammetry (CV) was performed using an electrochemical workstation (CHI660C, Shanghai Chenhua). The CV curves were recorded between 1.0 and 2.8 V at a scan rate of 0.1 mV s^{-1} at room temperature. The charge/discharge tests were performed using a battery tester (Neware CT-2001A, China) cycled between 1.0 and 3.0 V versus Li$^+$/Li unless otherwise specified at 0.1 C.

Results and discussion

Physical characteristics

The surface morphologies of pristine and Sn-doped TiO_2 nanotubes with different contents of Sn (3, 5, and 7 at.%) are illustrated in Fig. 1. It can be clearly observed that the surface of pristine, 3 and 5 at.% Sn-doped TiO_2, presents the morphology of smooth tube-like structure in a large field of view (Fig. 1a–c). Comparatively, the morphology of 7 at.% Sn-doped TiO_2 nanotube looks quite like bamboo joint structure (Fig. 1d), which may be originated from the influence of high content of tin doping. Although each image exhibits certain extent of aggregation, it is obvious that the nanotube dispersed better after tin doping.

The total pore volume values of pristine, 3, 5, and 7 at.% Sn-doped TiO_2 nanotubes, are 0.44, 0.47, 0.54, and 0.39 $cm^3\ g^{-1}$ according to the analysis based on the BJH method. Apparently, the excess doping makes the nanotubes like bamboo joint structure (Fig. 1d), which possibly reduces the space inside the nanotube. BJH pore size distributions for the samples demonstrate the presence of well-developed mesoporosity with narrow pore size distributions and a rather stable average pore diameter of 10 nm (not shown). The BET multipoint method was used to compare the specific areas of as-prepared samples. The measurement results show 108, 112, 122, and 139 $m^2\ g^{-1}$ for the doping ratios of pristine, 3, 5, and 7 at.%, respectively. Obviously, 7 at.% Sn-doped TiO_2 nanotube has the largest specific area, in accord with the structure of bamboo joint nanotube in Fig. 1d. This mesoporosity with high surface area may facilitate rapid diffusion during the electrochemical charge/discharge reaction, thereby enhancing the rate property of the material.

To further elucidate the microstructure in Fig. 1, TEM measurement was performed and shown in Fig. 2. The morphology of hollow tube is clearly revealed in Fig. 2a, with a diameter of about 10 nm and average length of 150 nm. As shown in Fig. 2b, the tube diameter and length keep unchanged after tin doping. Comparatively, the nanotube dispersed better after tin doping, corresponding with the SEM results in Fig. 1.

Figure 3 displays the XRD patterns of pristine and Sn-doped TiO_2 nanotubes. All the diffraction peaks could be indexed to the pure phase of anatase TiO_2 (JCPDS 21-1272). In the profiles of the different doping ratios of Sn-doped TiO_2 nanotubes, no diffraction peak from impurity can be observed. The calculated lattice parameters and grain sizes are shown in Table 1. Careful investigation shows that the diffraction peaks of Sn-doped TiO_2 nanotubes shifted to lower angles and that the lattice parameter is enlarged slightly with the increase of doping ratios, which possibly derives from the larger ionic radius of doped Sn^{4+} (0.069 nm) than Ti^{4+} (0.0606 nm) [19], indicating that the Sn^{4+} has successfully doped into the lattice of TiO_2. The grain sizes of the samples were calculated using

Fig. 1 SEM images of **a** pristine, **b** 3 at.%, **c** 5 at.%, and **d** 7 at.% Sn-doped TiO_2 nanotubes
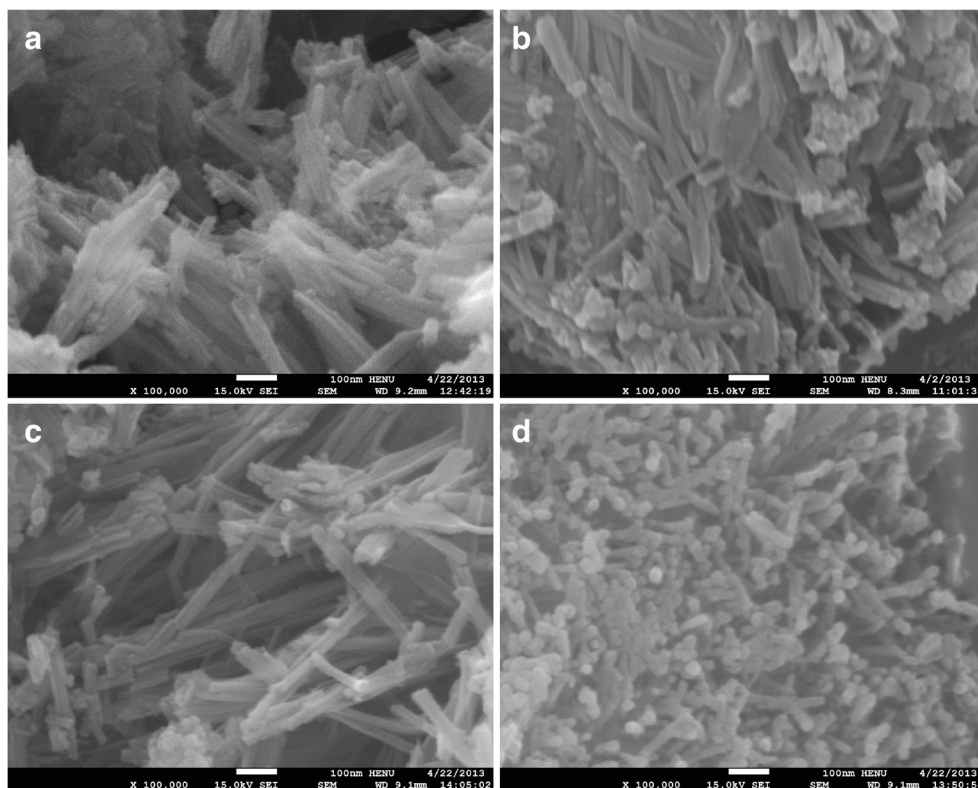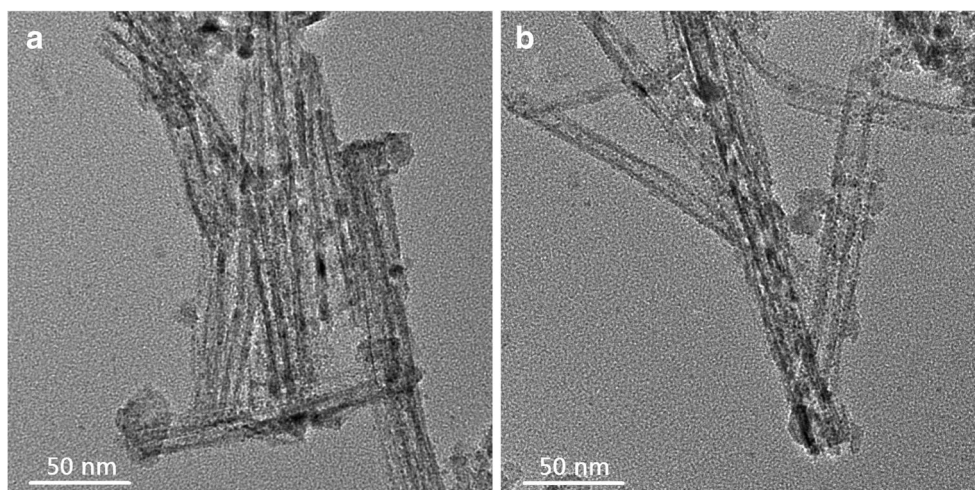
the Scherrer's formula, $D=K\lambda/\beta\cos\theta$ [21], where K is a constant (shape factor, about 0.89), λ is the X-ray wavelength, β is the full width at half-maximum (FWHM) in radians obtained using Jade software, and θ is the scattering angle. The results of grain sizes suggested that the doping process has little influence on the grain size of TiO_2. Additionally, it can be observed from Fig. 3 that the crystallinity increases in certain extent with the increase of Sn-doping amount, especially around 55°. Park et al. fabricated self-catalysis-grown SnO_2 anode and demonstrated the catalyst effect of Sn on material crystallization [22]. Other previous reports also approved that the anatase phase of TiO2 can be formed more rapidly due to the existence of tin [16, 17, 19, 23].

To reveal the subtle surface composition and structural information of a material, Raman spectra of pristine and Sn-doped TiO_2 nanotubes are collected and shown in Fig. 4. Five vibrational peaks at 142, 195, 395, 513, and 637 cm^{-1} with strong intensities can be clearly identified, which are in good agreement with the typical Raman characteristics of anatase TiO_2 [24–26]. Fitting results indicate that the FWHM of the 142-cm^{-1} mode has almost the same value in the resolution
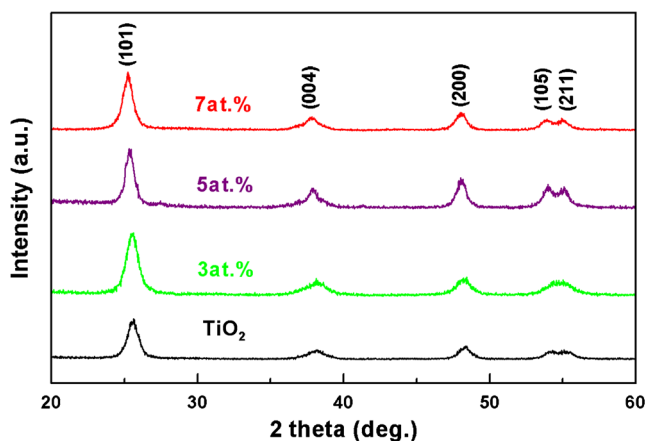
scope of Raman spectrometer. This certifies that crystallinity keeps unchanged after doping process, corresponding with the crystallite size analysis in Fig. 4.

The chemical composition and valence states of 5 at.% Sn-doped TiO_2 nanotubes were investigated by XPS, as shown in Fig. 5. Double peaks with BEs at 458.7 and 464.4 eV are shown in Fig. 5a, which correspond to Ti $2p_{1/2}$ and Ti $2p_{3/2}$ spin-orbit splitting peaks with a BE separation of 5.7 eV [27]. Figure 5b shows the smoothed profile of Sn 3d with BEs at 485.5 and 495.1 eV for $3d_{5/2}$ and $3d_{3/2}$, respectively. The results above clearly indicate that both Ti and Sn have quadrivalent oxidation state, which is in good agreement with previous literatures [28, 29]. The above analysis manifests that Sn^{4+} ions have successfully doped into the lattice of TiO_2, in consistent with the XRD results.

Hall effect measurement was carried out to investigate the influence of tin doping on the electronic conductivity of TiO_2 nanotube. As listed in Table. 2, all the samples exhibit features of n-type semiconductors. When the tin content is less than 5 at.%, doping remarkably enhances the electronic conductivity through increasing the number of free charge carriers and Hall mobility. When the content of tin further enhances from 5 to 7 at.%, both the carrier concentration and Hall mobility sharply decrease, which will inevitably deteriorate the conductivity of the corresponding material.

Fig. 3 XRD profiles of the pristine and Sn-doped TiO_2 nanotubes

Table 1 The calculated lattice parameters and grain sizes extracted from XRD results

Samples	a (Å)	b (Å)	c (Å)	Grain size (nm)
Pristine	3.754 (6)	3.754 (6)	9.255 (7)	12.5
3 at.%	3.767 (3)	3.767 (3)	9.266 (4)	12.7
5 at.%	3.776 (1)	3.776 (1)	9.277 (8)	13.3
7 at.%	3.788 (3)	3.788 (3)	9.280 (4)	13.1

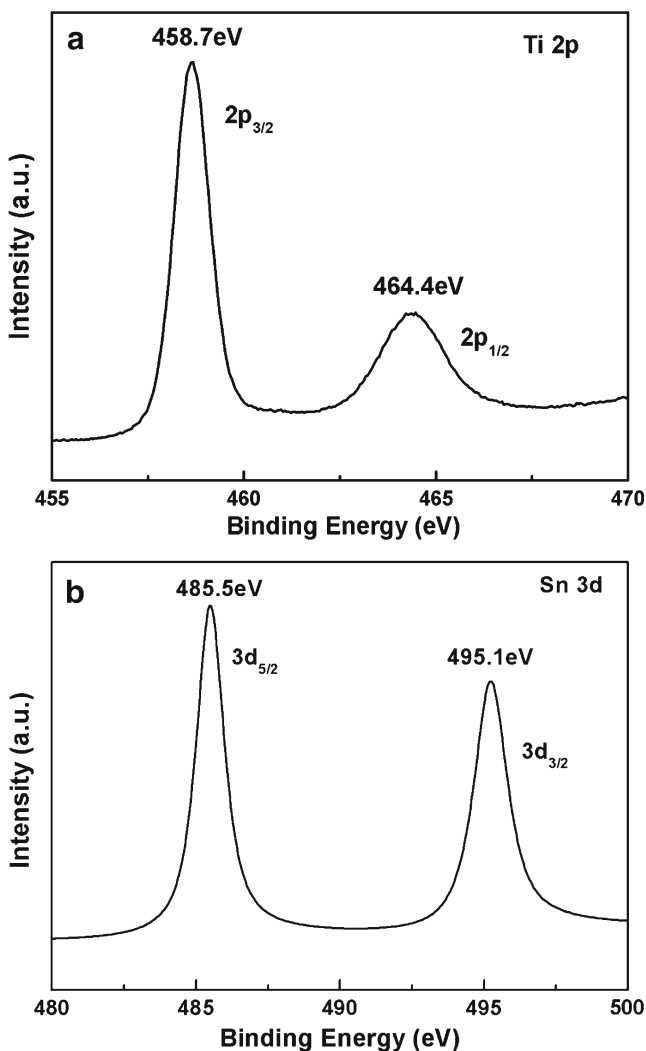Fig. 4 Raman spectra of pristine and Sn-doped TiO_2 nanotubes

Table 2 Hall measurement results of pristine and Sn-doped TiO_2 nanotubes

Samples	Carrier concentration/cm^{-3}	Hall mobility/$cm^2\ V^{-1}\ s^{-1}$
Pristine	2.16×10^{15}	11.18
3 at.%	1.30×10^{16}	20.64
5 at.%	1.91×10^{17}	19.08
7 at.%	2.46×10^{15}	9.09

Electrochemical characteristics

Figure 6a compares the charge specific capacities of pristine and Sn-doped TiO_2 nanotubes at 0.1 C between 1.0 and 3.0 V up to 50 cycles. As for pristine material, the capacity fades from 252 to 205 mAh g^{-1} after 50 cycles, with capacity retention of 81.3 %. After tin doping, the charge capacities decay from 324, 386, and 267 to 266, 342, and 207 mAh g^{-1} after 50 cycles, with capacity retentions of 82.1, 88.6, and

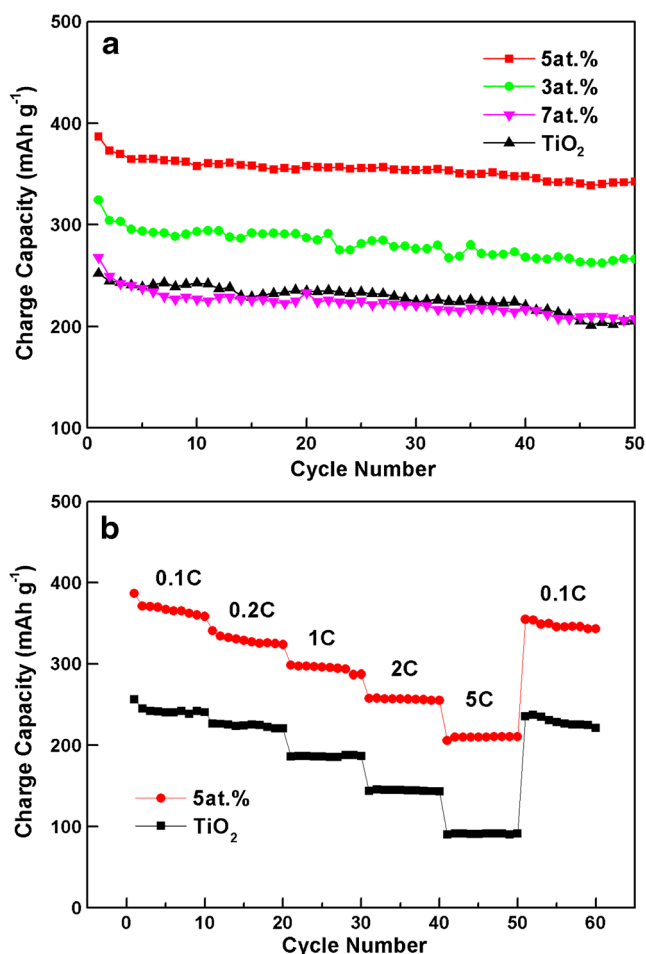Fig. 5 Binding energies of a Ti 2p and b the smoothed curve of Sn 3d for 5 at.% Sn-doped TiO_2 nanotube

Fig. 6 a Cycling performance of pristine and Sn-doped TiO_2 nanotubes between 1.0 and 3.0 V at room temperature. b Rate performance of pristine and 5 at.% Sn-doped TiO_2 nanotubes in the voltage range of 1.0–3.0 V at room temperature

77.5 % for the doping ratios of 3, 5, and 7 at.%, respectively. Apparently, TiO$_2$ nanotube with 5 at.% tin doping shows the best capacity retention.

The rate performances of pristine and 5 at.% Sn-doped TiO$_2$ nanotube were evaluated at different current densities in the voltage range of 1.0–3.0 V in Fig. 6b. Compared with pristine TiO$_2$ nanotube, 5 at.% Sn-doped TiO$_2$ nanotube exhibits much improved rate capability. In particular, it retained a high capacity of 210 mAh g^{-1} at 5 C. When the current density recovers to 0.1 C, the capacity increased to 341 mAh g^{-1} with stable cycling. Evidently, compared with pristine TiO$_2$ nanotube, 5 at.% Sn-doped TiO$_2$ nanotube exhibits much improved electrochemical performances.

The results in Fig. 6 indicate that appropriate doping ratio enhances the reversible capacity of the material, which may be attributed to the increased electronic conductivity (Table 2). Taking the physical characteristic results into account, when doping ratio is less than the optimal content, its role does not

be fully exerted. Once doping ratio exceeds the optimal content, microstructure of the sample may be greatly influenced, and the morphology of the sample turns to be like bamboo joint tubes (Fig. 1d), which possibly reduces the space inside the nanotube, as indicated by the pore volume analysis results. The reduced inside space of the nanotube alleviates the buffering effect on the volume change and accumulated stress in repeated alloying and dealloying. On the other hand, the conductivity of 5 at.% Sn-doped TiO$_2$ nanotube is higher than that of the others and therefore will result in a desirable reversibility of the material. The increase in the BET indicates more efficient contact between electrode and electrolyte, which is a benefit for lithium transportation in a certain extent. However, the decrease of electron carrier and Hall mobility hinders this positive effect of enhanced BET when the tin content reaches 7 at.%. Taking all the analysis above, it is not difficult to understand that 5 at.% Sn-doped TiO$_2$ exhibits the best electrochemical properties.
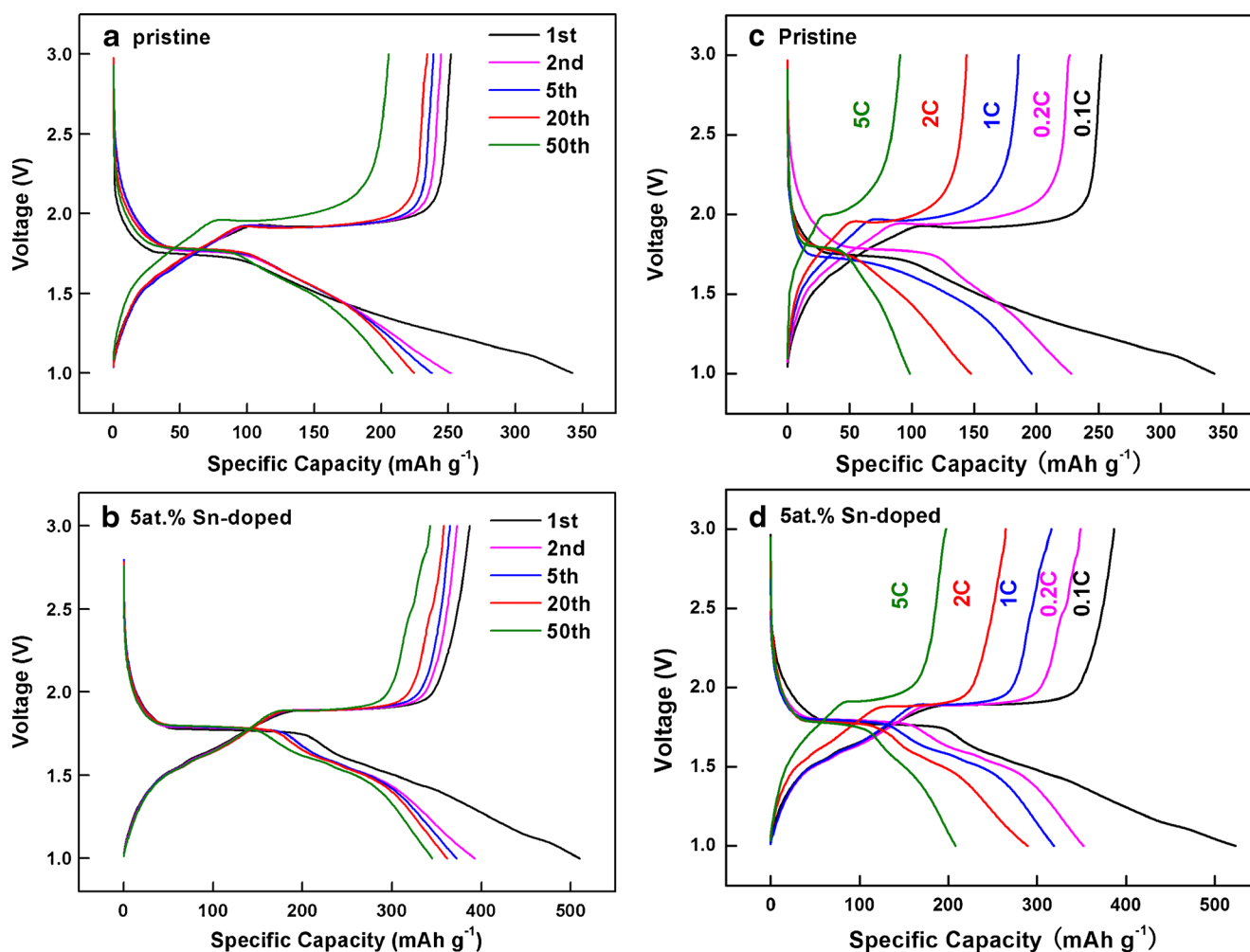

Fig. 7 Charge/discharge curves of **a** pristine, **b** 5 at.% Sn-doped TiO$_2$ nanotube at 0.1 C, **c** pristine, and **d** 5 at.% Sn-doped TiO$_2$ nanotube at different current rates

In order to compare the charge/discharge profiles of TiO2 nanotube after tin doping, the galvanostatic profiles of pristine TiO2 and 5 at.% Sn-doped TiO2 nanotube were displayed in Fig. 7. Figure 7a shows the charge/discharge profiles of anatase TiO2. It can be clearly observed that distinct discharge/charge plateaus locate at 1.75 and 2.0 V, which are characteristic of a two-phase electrochemical reaction [10, 30, 31]. The Li+ insertion/extraction reaction in TiO2 electrode can be written as the following:

$$TiO_2 + x\ Li^+ + x\ e \rightleftarrows Li_x TiO_2 \qquad (1)$$
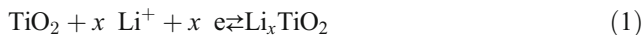
with the maximum insertion coefficient x usually close to 0.5 in anatase TiO2, and x is varied with different TiO2 polymorph, morphology, and crystallographic orientation [10, 32].

As shown in Fig. 7a, the initial discharge/charge capacity of TiO2 is 342 and 252 mAh g^{-1}, corresponding to a coulombic efficiency of 73.68 %. The capacity loss for the initial cycle is mainly attributed to the irreversible reduction of organic electrolyte [8, 33, 34] and large specific area of TiO2-induced side reactions [10, 35]. In comparison, Sn-doped TiO2 delivers an initial discharge/charge capacity of 510 and 386 mAh g^{-1}, leading to a coulombic efficiency of 75.68 % (Fig. 7b), higher than that of pristine TiO2. Figure 7c, d illustrates the charge/discharge profiles of pristine and 5 at.% Sn-doped TiO2 nanotube at different current rates. The charge/discharge plateau of TiO2 at different current rates remains consistent, indicating that appropriate doping does not change the anatase structure of pristine TiO2. As can be clearly observed in Table 2, the pristine material exhibits poor conductivity. Remarkably, the conductive property enhanced almost two magnifications after 5 at.% Sn doping.

CV profiles of pristine and 5 at.% Sn-doped TiO2 nanotube are shown in Fig. 8, in which the oxidation/reduction peaks locate at 2.0 and 1.75 V, corresponding with the characteristic redox of anatase TiO2, which is attributed to the reversible biphasic transition between tetragonal anatase and orthorhombic Li$_{0.5}$TiO2 [8, 10, 28, 29, 36, 37]. The stable redox of TiO2 before and after Sn doping indicates that appropriate doping does not change the anatase structure of pristine TiO2, which agrees with the XRD, Raman, and XPS results in Figs. 3, 4, and 5. Additionally, for 5 at.% Sn-doped TiO2 nanotube, the intensities of the oxidation/reduction peaks decay more slowly than those of the pristine material, resulting in better cycling stability, which is consistent with the results in Figs. 6 and 7.

Conclusions

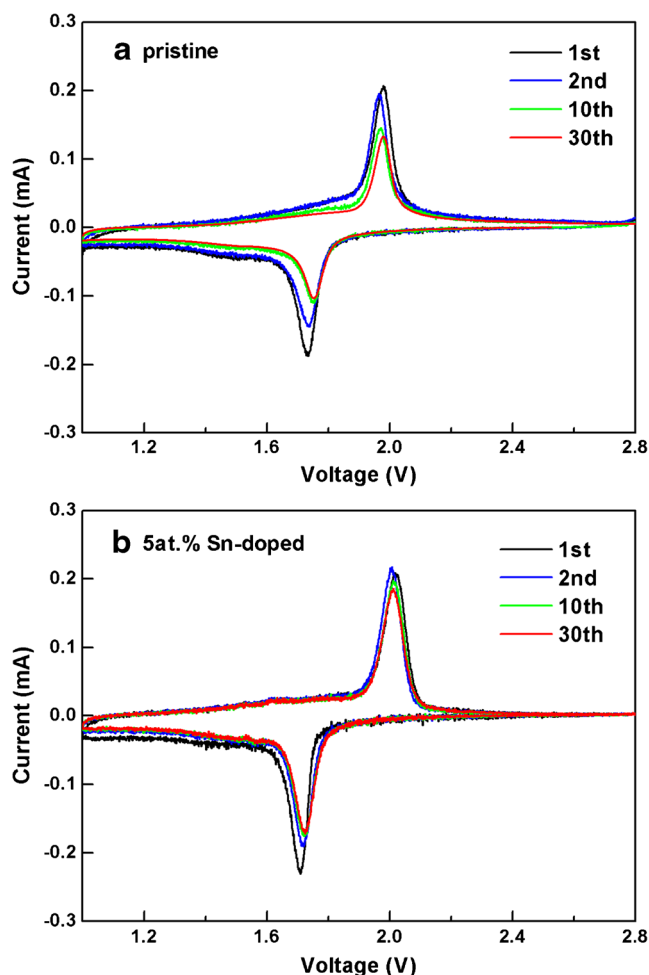Sn-doped TiO2 nanotubes were successfully synthesized through sol-gel and hydrothermal method. The phase,

Fig. 8 CV curves of **a** pristine and **b** 5 at.% Sn-doped TiO2 nanotubes at different cycles measured with a scan rate of 0.1 mV s^{-1} between 1.0 and 2.8 V at room temperature

component, and structure features of the as-prepared samples were carefully investigated and compared by various physical characterizations. Electrochemical tests show that 5 at.% Sn-doped TiO2 nanotube exhibits the optimal performances, which delivers a high-charge capacity of 342 mAh g^{-1} after 50 cycles and presents excellent rate performance. The enhanced electrochemical performances after 5 at.% Sn doping can be ascribed to the two magnification increases of electronic conductivity proved by Hall effect measurement, which is beneficial for the dynamic property of the material and therefore improves its reversibility in repeated cycling.

References

1. Haspert LC, Gillette E, Lee SB, Rubloff GW (2013) Energy Environ Sci 6:2578–2590
2. Yi TF, Li CY, Zhu YR, Shu J, Zhu RS (2009) J Solid State Electrochem 13:913–919
3. Liu R, Mahurin SM, Lee C, Unocic RR, Idrobo JC, Gao HJ, Pennycook SJ, Dai S (2011) Angew Chem Int Ed 50:6799–6802
4. Penki TR, Shanmughasundaram D, Munichandraiah N (2013) J Solid State Electrochem 17:3125–3136
5. Yang YQ, Bai Y, Zhao S, Chang QJ, Zhang WF (2013) J Alloys Compd 579:7–11
6. Wang XJ, Lee HS, Lee H, Yang XQ, Huang XJ (2010) Electrochem Commun 12:386
7. Wang FM, Yu MH, Hsiao YJ, Tsai Y, Hwang BJ, Wang YY, Wan CC (2011) Int J Electrochem Sci 6:1014–1026
8. Wang JP, Bai Y, Wu MY, Yin J, Zhang WF (2009) J Power Sources 191:614–618
9. Wu H, Zheng GY, Liu N, Carney TJ, Yang Y, Cui Y (2012) Nano Lett 12:904–909
10. Chen JS, Tan YL, Li CM, Chen YL, Luan D, Madhavi S, Boey FYC, Archer LA, Lou XW (2010) J Am Chem Soc 132:6124–6130
11. Javadekar A, Jayakumar A, Gorte RJ, Vohs JM, Buttrey DJ (2012) J Electrochem Soc 159(4):A386–A389
12. Mai LQ, Xu L, Han CH, Xu X, Luo YZ, Zhao SY, Zhao YL (2010) Nano Lett 10:4750–4755
13. Yue WB, Tao SS, Fu JM, Gao ZQ, Ren Y (2013) Carbon 65:97–104
14. Kyeremateng NA, Vacandio F, Sougrati MT, Martinez H, Jumas JC, Knauth P, Djenizian T (2013) J Power Sources 224:269–277
15. Etacheri V, Haik O, Goffer Y, Roberts GA, Stefan IC, Fasching R, Aurbach D (2012) Langmuir 28:965–976
16. Aldon L, Kubiak P, Picard A, Jumas JC, Fourcade JO (2006) Chem Mater 18:1401–1406
17. Issac I, Scheuermann M, Becker SM, Bardaji EG, Adelhelm C, Wang D, Kübel C, Indris S (2011) J Power Sources 196:9689–9695
18. Lü YJ, Zhang XX, Chen M (2013) J Phys Chem B 117:10241–10249
19. Shannon RD (1976) Acta Crystallogr 32:751–767
20. Kyeremateng NA, Hornebecq V, Knauth P, Djenizian T (2012) Electrochim Acta 62:192–198
21. Monshi A, Foroughi MR, Monshi MR (2012) J Nano Sci Eng 2:154–160
22. Park MS, Wang GX, Kang YM, Wexler D, Dou SX, Liu HK (2007) Angew Chem Int Ed 46:750–753
23. Harunsani MH, Freddy EO, Robert GP, Russell GE (2010) Chem Mater 22:1551–1558
24. Baddour-Hadjean R, Pereira-Ramos JP (2010) Chem Rev 110:1278
25. Li L, Yin X, Liu S, Wang Y, Chen L, Wang T (2010) Electrochem Commun 12:1383–1386
26. Reddya MV, Jose R, Teng TH, Chowdari BVR, Ramakrishna S (2010) Electrochim Acta 55:3109–3117
27. Han H, Song T, Bae JY, Nazar LF, Kim H, Paik U (2011) Energy Environ Sci 4:4532–4536
28. Yue WB, Yang S, Ren Y, Yang XJ (2013) Electrochim Acta 92:412–420
29. Harunsani MH, Oropeza FE, Palgrave RG, Egdell RG (2010) Chem Mater 22:1551–1558
30. Yang MC, Lee YY, Xu Y, Powers K, Meng YS (2012) J Power Sources 207:166–172
31. Fu LJ, Zhang T, Cao Q, Zhang HP, Wu YP (2007) Electrochem Commun 9:2140–2144
32. Zakharova GS, Jahne C, Popa A, Taeschner C, Täschner CH, Gemming T, Leonhardt A, Büchner B, Klingeler R (2012) J Phys Chem C 116:8714–8720
33. Li JR, Tang ZL, Zhang ZT (2005) Electrochem Solid-State Lett 8:A316
34. Xu JW, Wang YF, Li ZH, Zhang WF (2008) J Power Sources 175:903–908
35. Wang J, Zhou YK, Hu YY, O'Hayre R, Shao ZP (2011) J Phys Chem C 115:2529–2536
36. Ortiz GF, Hanzu I, Djenizian T, Lavela P, Tirado JL, Knauth P (2009) Chem Mater 21:63–67
37. Dambournet D, Belharouak I, Amine K (2010) Chem Mater 22:1173–1179